

NGC454: unveiling a new “changing look” AGN

E. Marchese^{1, 2*}, V. Braito^{1, 3†}, R. Della Ceca¹, A. Caccianiga¹, P. Severgnini¹

¹INAF-Osservatorio Astronomico di Brera, via Brera 28, 20121 Milano, Italy

²Università degli studi di Milano-Bicocca, Piazza dell’Ateneo Nuovo, 1 - 20126, Milano

³X-Ray Astronomy Observational Group, Department of Physics and Astronomy, Leicester University, Leicester LE1 7RH, UK

ABSTRACT

We present a detailed analysis of the X-ray spectrum of the Seyfert 2 galaxy NGC454E, belonging to the interacting system NGC454. Observations performed with *Suzaku*, *XMM-Newton* and *Swift* allowed us to detect a dramatic change in the curvature of the 2–10 keV spectrum, revealing a significant variation of the absorbing column density along the line of sight (from $\sim 1 \times 10^{24} \text{cm}^{-2}$ to $\sim 1 \times 10^{23} \text{cm}^{-2}$). Consequently, we propose this source as a new member of the class of “changing look” AGN, i.e. AGN that have been observed both in Compton-thin ($N_{\text{H}}=10^{23} \text{cm}^{-2}$) and reflection dominated states (Compton-thick, $N_{\text{H}} > 10^{24} \text{cm}^{-2}$). Due to the quite long time lag (6 months) between the *Suzaku* and *XMM-Newton* observations we cannot infer the possible location of the obscuring material causing the observed variability. In the 6–7 keV range the *XMM-Newton* observation also shows a clear signature of the presence of an ionized absorber. Since this feature is not detected during the *Suzaku* observation (despite its detectability), the simplest interpretation is that the ionized absorber is also variable; its location is estimated to be within $\sim 10^{-3}$ pc from the central black hole, probably much closer in than the rather neutral absorber.

Key words: galaxies: active – galaxies: individual (NGC454) – X-rays: galaxies

1 INTRODUCTION

There is now a general consensus that Active Galactic Nuclei (AGN) are powered by accretion of matter onto a supermassive black hole (SMBH), located at center of almost all massive galaxies. It is also clear that, according to the Unified Model of AGN (Antonucci 1993), the difference between type 1 and type 2 AGN can be explained through orientation effects between our line of sight to the nucleus and “circum-nuclear material”. However, the geometry, size and physical state of this circum-nuclear matter are still a matter of debate. In particular, the AGN X-ray spectra are complex and consist of multiple components (see Turner & Miller 2009, Done 2010 for a review), which are all intimately related to the still poorly understood condition of the matter near the nucleus. This circum-nuclear gas imprints features - low energy cut-offs, the Compton hump and emission and absorption lines - onto the primary X-ray emission. The X-ray spectra and, crucially, their variability observed in few nearby AGN showed that this matter is highly structured with a range of ionisation states, densities, geometries and locations (Turner & Miller 2009, Risaliti 2010). In this respect, the significant variability of the absorbing column density (N_{H}) detected in the so called “changing look” AGN, i.e. AGN that have been observed both in Compton-thin ($N_{\text{H}}=10^{23} \text{cm}^{-2}$)

and reflection dominated states ($N_{\text{H}} > 10^{24} \text{cm}^{-2}$) (Risaliti et al. 2002), implies that the absorbing material has to be clumpy and at much smaller distance than the conventional obscuring “torus” with velocity, distance and size from the central X-ray source of the same order of those of the Broad Line Region (BLR) clouds.

Up to now, we can count only a few “changing look” AGN where such a variability has been discovered on time-scales from a few days down to a few hours: NGC 1365 (Risaliti et al. 2005, 2007, 2009), NGC 4388 (Elvis et al. 2004), NGC 7674 (Bianchi et al. 2005), NGC 4151 (Puccetti et al. 2007), NGC 7582 (Bianchi et al. 2009), UGC 4203 (Risaliti et al. 2010), NGC4051 (Uttley et al. 2004; Lobban et al. 2011) and 1H 0419-577 (Pounds et al. 2004). Among them we recall NGC2992 (Weaver et al. 1996), however for this source one year monitoring with RXTE (Murphy et al. 2007) unveiled the presence of short-term flaring activity rather than a change in the covering of the absorber.

Within a project investigating the occurrence of AGN in a sample of interacting galaxies, we came across an interacting system, NGC454, which was recently observed in the X-ray energy band with *Suzaku*, and ~ 6 months later with *XMM-Newton*, and whose main X-ray spectral components present interesting variability properties.

Here we compare and discuss the X-ray observations from *Suzaku*, *XMM-Newton* and *Swift* that unveiled that NGC454 can

* E-mail: elena.marchese@brera.inaf.it

† E-mail: valentina.braito@brera.inaf.it

be placed among those AGN whose absorbing N_{H} is strongly variable (section 4.2). The paper is structured as follows. The interacting system NGC454 is described in §2. The X-ray observations and data reduction are summarized in §3. In §4 we present the spectral analysis of both datasets and the comparison between the observations, aimed to assess the nature of the X-ray absorber. Summary and conclusions follow in §5.

Throughout this paper, a concordance cosmology with $H_0 = 71 \text{ km s}^{-1} \text{ Mpc}^{-1}$, $\Omega_{\Lambda}=0.73$, and $\Omega_m=0.27$ (Spergel et al. 2003) is adopted.

2 NGC454

Optical studies (Arp & Madore 1987; Johansson 1988; Stiavelli et al. 1998) of the interacting system NGC454 (see Figure 1, right panel) describe it as a pair of emission line galaxies consisting of a red elliptical galaxy (eastern component, hereafter NGC454E) and a blue irregular galaxy (western component, hereafter NGC454W), at redshift $z=0.0122$. The distorted morphology of both these galaxies, together with the spectroscopic and photometric evidence of a young stellar population, is a clear sign of the interacting nature of this system. Furthermore, three very blue knots (discussed in section 3.3.1), probably Strongren spheres surrounding clusters of very hot newly formed stars, are located (and likely related) to the south of NGC454W. *HST* observations of the system, performed with the Wide Field Planetary Camera 2, confirmed that NGC454 is in the early stages of interaction (Stiavelli et al. 1998). The above authors stated also that an important fraction of gas has drifted to the center of the eastern component, but it has yet not produced any significant visible star formation activity; a population of young star clusters has formed around the western component.

The optical spectrum of NGC454E is consistent with that of a Seyfert 2 galaxy (although none of the high excitation lines, e.g. HeII lines, can be seen) while no optical evidence of an AGN is present in the spectrum of NGC454W which is fully consistent with that of a star-forming galaxy (Johansson 1988).

3 OBSERVATIONS AND DATA REDUCTION

3.1 *Suzaku* data

NGC454 was observed on April 29, 2009 by the Japanese X-ray satellite *Suzaku* (Mitsuda et al. 2007) for a total exposure time of about 130 ksec. *Suzaku* carries on board four X-ray Imaging Spectrometers (XIS, Koyama et al. 2007), with X-ray CCDs at their focal plane, and a non-imaging hard X-ray detector (HXD-PIN, Takahashi et al. 2007). At the time of this observation only three of the XIS were working: one back-illuminated (BI) CCD (XIS1) and two front-illuminated (FI) CCDs (XIS0 and XIS3). All together the XIS and the HXD-PIN cover the 0.5–10 keV and 12–70 keV bands respectively. The spatial resolution of the XIS is ~ 2 arcmin (HEW), while the field of view (FOV) of the HXD-PIN is 34 arcmin radius. Data from the XIS and HXD-PIN were processed using v2.1.6.14 of the *Suzaku* pipeline and applying the standard screening parameters¹.

¹ The screening filters all events within the South Atlantic Anomaly (SAA) as well as with an Earth elevation angle (ELV) $< 5^\circ$ and Earth day-time elevation angles (DYE_ELTV) less than 20° . Furthermore also data within

3.1.1 The *Suzaku* XIS analysis

The XIS data were selected in 3×3 and 5×5 editmodes using only good events with grades 0,2,3,4,6 and filtering the hot and flickering pixels with the script *siscclean*; the net exposure times are 103 ksec for each of the XIS. The XIS source spectra were extracted from a circular region of $2.2'$ radius centered on the source, and the background spectra were extracted from two circular regions with the same radius of the source region, offset from the source and the calibration sources. The XIS response (rmfs) and ancillary response (arfs) files were produced, using the latest calibration files available, with the *ftools* tasks *xisrmfgen* and *xissimarfgen* respectively. The spectra from the two FI CDDs (XIS 0 and XIS 3) were combined to create a single source spectrum (hereafter XIS-FI), while the BI (the XIS1) spectrum was kept separate and fitted simultaneously. The net 0.5–10 keV count rates are: $(0.0117 \pm 0.0005) \text{ cts/s}$, $(0.0142 \pm 0.0005) \text{ cts/s}$, $(0.0132 \pm 0.0006) \text{ cts/s}$ for the XIS0, XIS3 and XIS1 respectively. We considered data in the range 0.5–10 keV for the XIS-FI and in the range 0.6–7 keV for the XIS-BI (because the XIS-BI is optimized for observing below ~ 7 keV). For both the XIS-FI and XIS-BI we ignored the band 1.6–1.9 keV, due to the presence of instrumental calibration uncertainties. The net XIS source spectra were then binned to a minimum of 50 counts per bin.

3.1.2 The *Suzaku* HXD-PIN analysis

For the HXD-PIN data reduction and analysis we followed the latest *Suzaku* data reduction guide (the ABC guide Version 2²), and used the rev2 data, which include all 4 cluster units. The HXD-PIN instrument team provides the background (known as the “tuned” background) event file, which accounts for the instrumental “Non X-ray Background” (NXB; Kokubun et al. 2007). The systematic uncertainty of this “tuned” background model is $\pm 1.3\%$ (at the 1σ level for a net 20 ksec exposure³).

We extracted the source and background spectra using the same common good time interval, and corrected the source spectrum for the detector dead time. The net exposure time after the screening was 106 ksec. We then simulated a spectrum for the cosmic X-ray background counts (Boldt 1987; Gruber et al. 1999) and added it to the instrumental one.

NGC454 is detected at a level of 3.4 % above the background and the net count rate in the 15–30 keV band is $0.01 \pm 0.002 \text{ cts/s}$. For the spectral analysis the source spectrum was rebinned in order to have a signal-to-noise ratio ≥ 3 in each energy bin. We fit the *Suzaku*-HXD spectrum with a single absorbed power-law component with a photon index $\Gamma = 1.9$ and derived an observed 15–30 keV flux of $\sim 3.4 \times 10^{-12} \text{ erg cm}^{-2} \text{ s}^{-1}$.

3.2 The *Swift*-BAT observation

NGC454 was also detected with the BAT detector on board of *Swift* (Gehrels et al. 2004). BAT is a coded aperture imaging camera that operates in the 14–150 keV energy range; it has a large field of view (1.4 steradian half coded), and a point spread function (PSF) of 18 arcmin (HEW). *Swift*-BAT is devoted mainly

256s of the SAA were excluded from the XIS and within 500s of the SAA for the HXD. Cut-off rigidity (COR) criteria of $> 8 \text{ GV}$ for the HXD data and $> 6 \text{ GV}$ for the XIS were used.

² <http://heasarc.gsfc.nasa.gov/docs/suzaku/analysis/abc/>

³ <ftp://legacy.gsfc.nasa.gov/suzaku/doc/hxd/suzakumemo-2008-03.pdf>

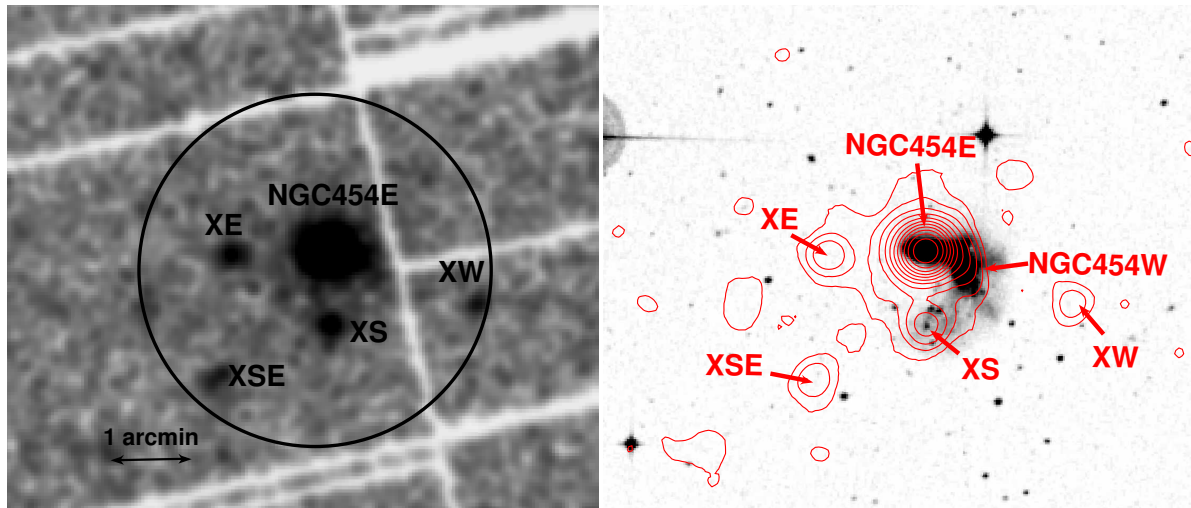


Figure 1. Left panel: XMM-Newton EPIC-pn image (0.5–10 keV) with superimposed the *Suzaku* XIS extraction region. Right Panel: *Digital Sky Survey* (DSS) optical image with overlaid the XMM-Newton PN 0.5–10 keV contours. We marked the main X-ray sources discussed in the text. It is evident that the main X-ray source is positionally coincident with NGC454E (classified as a Seyfert 2) while no X-ray emission is detected at the position of NGC454W.

to the monitoring of a large fraction of the sky for the occurrence of gamma ray bursts (GRBs); while waiting for new GRBs, it continuously collects spectral and imaging information in survey mode, covering a fraction between 50% and 80% of the sky every day.

NGC454 (BAT name: SWIFT J0114.4-5522) is part of the Palermo *Swift*-BAT 54-Month hard X-ray catalogue (Cusumano et al. 2010) and the *Swift*-BAT 58-Month Hard X-ray Survey (heasarc.gsfc.nasa.gov/docs/swift/results/bs58mon/).

This last survey detected 1092 sources in the 14–195 keV band down to a significance level of 4.8σ , reaching a flux level of $1.1 \times 10^{-11} \text{ erg cm}^{-2} \text{ s}^{-1}$ over 50% of the sky (and $1.48 \times 10^{-11} \text{ erg cm}^{-2} \text{ s}^{-1}$ over 90% of the sky); as part of this new edition of the Swift-BAT catalogue, 8-channel spectra and monthly-sampled light curves for each object detected in the survey were made available (Baumgartner et al. 2011).

The 14–195 keV observed flux of NGC454 is $1.90^{+0.5}_{-0.5} \times 10^{-11} \text{ erg cm}^{-2} \text{ s}^{-1}$, in agreement, when accounting for the different bands, with the flux quoted in the Cusumano et al. 2010 catalogue ($F_{14-195 \text{ keV}} \sim 1.7 \times 10^{-11} \text{ erg cm}^{-2} \text{ s}^{-1}$). This flux is also in good agreement with the expected 14–195 keV flux ($\sim 1.6 \times 10^{-11} \text{ erg cm}^{-2} \text{ s}^{-1}$) extrapolated from that measured with *Suzaku* in the 15–30 keV range.

3.3 The XMM-Newton observation

NGC454 was observed with XMM-Newton on November 5, 2009 for a total exposure time of about 30 ksec. The XMM-Newton Observatory (Jansen et al. 2001) carries, among its onboard instruments, three 1500 cm^2 X-ray telescopes, each with EPIC (European Photon Imaging Camera) imaging spectrometers at the focus. Two of the EPIC use MOS CCDs (Turner et al. 2001) and one uses a pn CCD (Strüder et al. 2001). These CCDs allow observations in the range ~ 0.5 –10 keV. The spatial resolution of the 2 MOSs is $\sim 14''$ (HEW), and $\sim 15''$ (HEW) for the pn (Ehle et al. 2001).

During this observation the pn, MOS1, and MOS2 cameras had the medium filter applied and they were operating in full frame Window mode. The data have been processed and cleaned using the

Science Analysis Software (SAS ver. 6.5) and analysed using standard software packages (FTOOLS ver. 6.1 and XSPEC ver. 11.3). Event files have been filtered for high-background time intervals, and only events corresponding to patterns 0–12 (MOS1, MOS2) and to patterns 0–4 (pn) have been used. The net exposure times at the source position after data cleaning are ~ 23.9 ksec (pn), ~ 29.1 ksec (MOS1) and ~ 29.2 ksec (MOS2).

In the right panel of Figure 1 we report the optical DSS image of the system NGC454, together with the XMM-Newton 0.5–10 keV contours (green, in the electronic version only) from EPIC-pn. It is evident that the bulk of the X-ray emission is positionally coincident with NGC454E (the galaxy spectroscopically classified as a Seyfert 2) while no strong X-ray emission is detected at the position of NGC454W (the source spectroscopically classified as a star-forming galaxy). We also detected a weak X-ray source to the south of NGC454, which is positionally coincident with one of the three very blue knots discussed above, likely a star forming region belonging to NGC454W.

The pn, MOS1 and MOS2 source spectra were extracted from a circular region of 0.46 arcmin radius centered on the source (NGC454E), while the background spectra were extracted from two circular regions with 0.5 arcmin radius offset from the source. The MOS1 and MOS2 spectra were combined, then both the EPIC-pn and EPIC-MOS spectra were grouped with a minimum of 30 counts per channel.

3.3.1 Contamination from unresolved sources in the *Suzaku* (XIS, HXD) and *Swift*-BAT extraction region/field of view

In the left panel of Figure 1 we show the XMM-Newton 0.5–10 keV pn image along with the *Suzaku* extraction region (circle with $2.2'$ radius). As discussed above the main X-ray source is centered on NGC454E but given the XMM-Newton better angular resolution ($14''$ – $15''$ HEW) as compared to *Suzaku* ($120''$ HEW), we can clearly distinguish 4 other X-ray sources, besides NGC454E, entering in the *Suzaku* XIS extraction region. We extracted the XMM-Newton spectra for the 3 brighter sources (XS, XE and XSE, marked in Figure 1 for clarity) and analysed them in order

to estimate their possible contribution to the *Suzaku* spectrum; the remaining source (XW) has only ~ 80 counts detected in the $\sim 0.5 - 10$ keV band (see below).

XS is well fitted with a power law, modified only by Galactic absorption, with a photon index $\Gamma \sim 1.8$ and a 2–10 keV flux $F_{[2-10]\text{keV}} \sim 1.9 \times 10^{-14} \text{ erg cm}^{-2} \text{ s}^{-1}$; the extrapolated flux in the 14–70 keV band (assuming $\Gamma \sim 1.8$) is $F_{[14-70]\text{keV}} \lesssim 3 \times 10^{-14} \text{ erg cm}^{-2} \text{ s}^{-1}$. As said above this source is likely associated with a star forming region related to NGC454W; if so, assuming $z = 0.0122$, its 2–10 keV luminosity is $L_{[2-10]\text{keV}} \sim 6.2 \times 10^{39} \text{ erg s}^{-1}$. We cannot establish if this luminosity is due to one or more sources and thus speculate on its/their nature, because we lack both the spatial resolution and a good enough sampling to assess its variability and spectral properties. The source to the east of NGC454E (hereafter XE) can be fitted with a power-law and a thermal component, yielding $\Gamma \sim 1.6$, $kT \sim 0.3$ and $F_{[2-10]\text{keV}} \sim 8.8 \times 10^{-15} \text{ erg cm}^{-2} \text{ s}^{-1}$ ($F_{[14-70]\text{keV}} \lesssim 5 \times 10^{-14} \text{ erg cm}^{-2} \text{ s}^{-1}$). The source to the south-east of NGC454E (hereafter XSE) can be fitted with an absorbed power law ($N_{\text{H}} \sim 2.2 \times 10^{22} \text{ cm}^{-2}$) with photon index set to 1.8 and $F_{[2-10]\text{keV}} \sim 2.7 \times 10^{-14} \text{ erg cm}^{-2} \text{ s}^{-1}$ ($F_{[14-70]\text{keV}} \lesssim 3 \times 10^{-14} \text{ erg cm}^{-2} \text{ s}^{-1}$). Finally, the fourth source located to the west of NGC454E (hereafter XW) has not enough counts for a meaningful spectral analysis (~ 80 counts) and its estimated fluxes are $F_{[2-10]\text{keV}} \sim 2.0 \times 10^{-14} \text{ erg cm}^{-2} \text{ s}^{-1}$ and $F_{[14-70]\text{keV}} \lesssim 2.5 \times 10^{-14} \text{ erg cm}^{-2} \text{ s}^{-1}$ (adopting $\Gamma \sim 1.9$). According to the extragalactic logN-logS distributions computed by Mateos et al. (2008), at this flux level the number of random 2–10 keV sources in the *Suzaku* extraction region is ~ 2 , thus the sources XE, XSE and XW are probably those expected by “chance”. There is no NED identification available for XE, XSE and XW.

The combined 2–10 keV flux of all these 4 possible contaminating sources ($F_{[2-10]\text{keV}} \sim 7.5 \times 10^{-14} \text{ erg cm}^{-2} \text{ s}^{-1}$) imply that they will provide a negligible contribution to the *Suzaku* XIS spectrum of NGC454 ($F_{[2-10]\text{keV}} \sim 6 \times 10^{-13} \text{ erg cm}^{-2} \text{ s}^{-1}$). More important their estimated $F_{[14-70]\text{keV}}$ are well below the *Suzaku* HXD-PIN or Swift-BAT sensitivity. On the other hand this check is still not sufficient for these two latter instruments since their FOV is larger than that of the *Suzaku* XIS instrument. Assuming that the X-ray emission above 10 keV detected with the HXD-PIN or the Swift-BAT is associated to the same source, as the good agreement of the measured fluxes strongly suggests, we can use the instrument with the smaller FOV (*Swift*-BAT) to perform further checks. In particular using known catalogues or archives (NED⁴ and SIMBAD⁵) we searched for bright X-ray/optical sources within 6 arcmin radius error circle (corresponding to 99.7% confidence level for a source detection at 4.8 standard deviations, Cusumano et al. 2010) that could be responsible of the observed X-ray emission above 10 keV. No plausible contaminant source was found and, in the following, we will assume that the emission above 10 keV comes from NGC454E. We note that we are also assuming a negligible contribution to the emission above 10 keV from the companion galaxy in the interacting system, NGC454W. While a confirmation of this assumption has to wait for direct imaging observations above 10 keV with adequate

spatial resolution, we stress that no emission was detected below 10 keV from NGC454W, while a contribution would be expected even in the case of a deeply buried AGN (see e.g. Della Ceca et al. 2002). We thus conclude that we do not expect significant contaminations from the nearby sources to the *Suzaku* and *Swift* spectra.

4 SPECTRAL ANALYSIS

4.1 The *Suzaku* and *Swift* broad band X-ray emission

We first considered the X-ray spectrum of NGC454E in the 0.5–100 keV band by fitting simultaneously the *Suzaku* XIS, *Suzaku* HXD and *Swift*-BAT data. The cross-normalisation factor between the HXD and the XIS-FI was set to 1.18, as recommended for HXD nominal observation processed after 2008 July (Manabu et al. 2007; Maeda et al. 2008⁶), while the cross-normalisation between *Swift* and XIS was allowed to vary.

In the subsequent sections the χ^2 statistics was used for the fit, the errors are quoted to 90% confidence level for 1 parameter of interest and all the spectral parameters are quoted in the rest frame of the source.

We fitted the continuum with a redshifted unabsorbed power-law model, modified only by Galactic ($N_{\text{H}} = 2.73 \times 10^{20} \text{ cm}^{-2}$, Dickey & Lockman 1990) absorption. This model did not provide an adequate description of the broadband spectrum of NGC454E ($\chi^2/\text{dof} = 522.6/122$). If we fit only the 2–5 keV continuum, excluding possible complexity in the soft energy range and near the Fe K emission line complex we found a very flat photon index ($\Gamma \sim 0.15$), strongly suggesting that we are dealing with an absorbed AGN, in agreement with the optical spectral classification of NGC454E.

The residuals with respect to this simple unabsorbed power-law model, which are shown in Figure 2, allowed us to infer the main features of the observed spectrum. An excess at energies below 1 keV, an emission line feature at ~ 6.4 keV (likely associated with Fe K α), together with a line-like feature at ~ 7 keV, and an excess at energies between 10 and 20 keV are clearly evident. The residuals in the soft X-rays suggest the presence of a thermal component probably related to the host galaxy. The simultaneous occurrence of a strong Fe K α emission line at ~ 6.4 keV (figure 2 upper and lower panel), a very flat observed Γ and an excess in the hard X-rays (above 10 keV) is the distinctive spectral signature of a highly absorbed source, with a possible strong Compton reflected component. The excess observed at ~ 7 keV (Figure 2 lower panel) is likely due to the combination of the Fe K β emission line (7.06 keV) and the Fe XXVI (~ 6.97 keV) and the Fe edge (~ 7.11 keV).

Given these features, we performed a broadband fit including:

- (i) a thermal component (modelled with the MEKAL model, Mewe et al. 1986);
- (ii) an absorbed primary power-law component;
- (iii) an unabsorbed power-law component with the same photon index Γ ;

⁴ <http://ned.ipac.caltech.edu/>

⁵ <http://simbad.u-strasbg.fr/simbad/>

⁶ <http://www.astro.isas.jaxa.jp/suzaku/doc/suzakumemo/suzakumemo-2007-11.pdf>;

<http://www.astro.isas.jaxa.jp/suzaku/doc/suzakumemo/suzakumemo-2008-06.pdf>

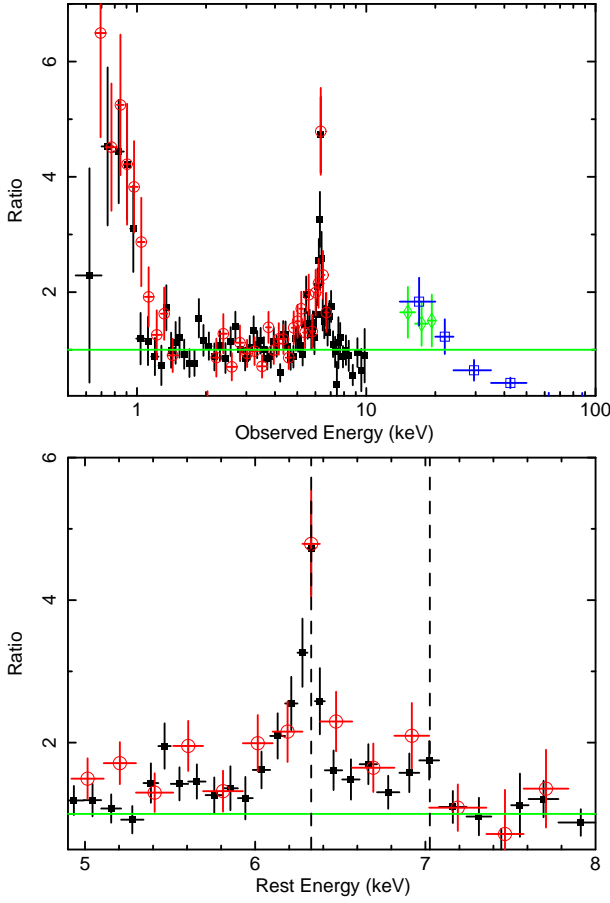


Figure 2. Upper panel: ratio between the *Suzaku* and *Swift* data (XIS-FI: black filled squares; XIS1: red open circles; HXD: green rhombs; and BAT: blue open squares, colors in the electronic version only) and the unabsorbed power-law model used to fit *Suzaku* data in the 2–5 keV energy range. Lower panel: zoom into the 5–8 keV energy range (XIS-FI: black filled squares, XIS1: red open circles). We can clearly see at 6.4 keV the excess characteristic of the Fe K α emission line and at ~ 7 keV, the combined contribution of the Fe K β emission line (7.06 keV), Fe XXVI (~ 6.97 keV), and the reflector edge. The central energies of the Fe K α and Fe K β are marked with dashed vertical lines.

(iv) two Gaussian emission lines at ~ 6.4 keV (Fe K α) and 7.06 keV (Fe K β) respectively. We kept the energy of the Fe K β fixed to 7.06 keV, tied its intrinsic width (σ) to the width of the corresponding Fe K α line and fixed its flux to be 13% of the Fe K α flux, consistent with the theoretical value (Kaastra & Mewe 1993);

(v) a Compton reflected component, modelled with the PEXRAV model in XSPEC (Magdziarz & Zdziarski 1995). The parameters of the reflected component are: an inclination angle i fixed to 63° , abundance $Z=Z_\odot$, a reflection fraction (defined by the subtending solid angle of the reflector $R = \Omega/4\pi$) fixed to be -1 (i.e. pure reflection)⁷, the cut-off energy (fixed at 200 keV, Dadina 2008) and the normalisation.

The absorber was modelled by a combination of the CABS and ZPHABS models in XSPEC, assuming the same column density,

⁷ Since in the “pure reflection” PEXRAV model there is a degeneracy between R and the normalisation, we set the reflection scaling factor to -1 and allowed the normalisation to vary.

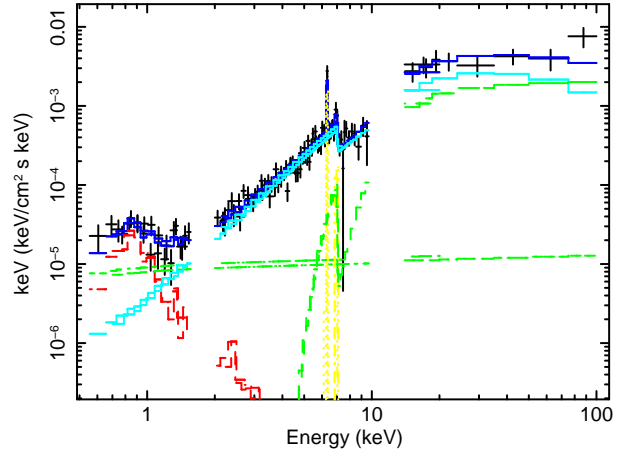


Figure 3. Unfolded *Suzaku* spectrum, showing separately the different components of the best-fit model: in green (in the electronic version) the scattered power-law and the primary absorbed power-law, in red (in the electronic version) the soft thermal component, in yellow (in the electronic version) the iron K α and K β emission lines, in light blue (in the electronic version) the reflection component, and in blue (in the electronic version) the total resulting spectrum.

since they represent the same medium producing two different effects (i.e. the non-relativistic Compton scattering and photoelectric absorption of the primary radiation, respectively).

The model setup is:

$$\text{WABS} \times [\text{MEKAL} + \text{ZPOWERLW} + \text{ZGAUSS} + \text{ZGAUSS} + \text{PEXRAV} + \text{CABS} \times \text{ZPHABS} \times (\text{ZPOWERLW})]$$

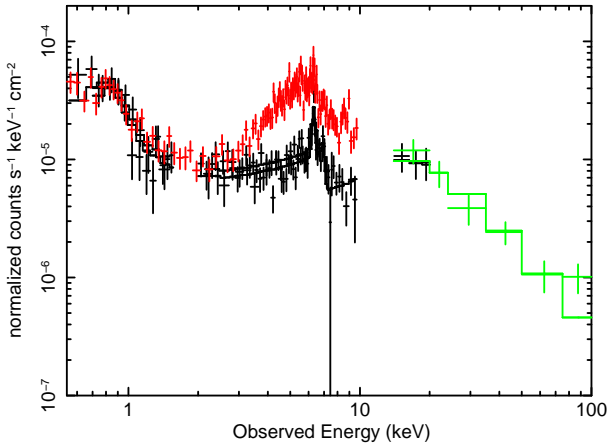
We found that this model provides a good representation of the X-ray emission of NGC454E ($\chi^2/\text{dof}=104.5/103$). The resulting best-fit parameters are reported in table 1. In particular, this best-fit model yielded $\Gamma = 1.92^{+0.29}_{-0.36}$, $N_H = 2.05^{+4.25}_{-1.38} \times 10^{24} \text{ cm}^{-2}$. The rest-frame energy of the Fe K α is $E_{K\alpha} = 6.38 \pm 0.02$ keV and its equivalent width with respect to the observed continuum is $\text{EW} = 340^{+60}_{-80} \text{ eV}$. At the *Suzaku* spectral resolution this emission line is unresolved; leaving the width σ free to vary we found $\sigma \lesssim 70$ eV (at the 90% confidence level), thus we fixed it to be $\simeq 10$ eV. The cross-normalisation factor between the *Swift*-BAT and the XIS-FI is $1.05^{+0.64}_{-0.39}$. We stress that a different choice of the cut-off energy in the range between 100 and 300 keV does not affect significantly the best-fit reflection parameters obtained in this work. f The relative importance of the reflection component is given by the ratio between the normalizations of the primary absorbed power-law and the reflection component; in our case this ratio is ~ 0.5 , which at first order would correspond to a reprocessor covering a solid angle 2π . The fraction of scattered radiation is $\sim 1\%$. The observed 2–10 keV flux is $\sim 6.3 \times 10^{-13} \text{ erg cm}^{-2} \text{ s}^{-1}$ while the intrinsic 2–10 keV luminosity obtained with this model is $7.2 \times 10^{42} \text{ erg s}^{-1}$.

4.2 Comparison with XMM-Newton data

In Figure 4 we report the *Suzaku* XIS (black, lower spectrum), HXD (black) and *Swift*-BAT spectra (green, in the electronic version only). In red (upper spectrum) we also show the XMM-Newton pn and MOS data, revealing a dramatic change in the spectral curvature between 3 and 6 keV. This variation is most likely due to a change in the amount of absorption of the primary radiation. To test this hypothesis we applied the *Suzaku* best-fit model to the XMM-

Table 1. Summary of the *Suzaku* and XMM-Newton parameters for the best-fit models described in section 4.1, and 4.2.1.

Model Component	Parameter	<i>Suzaku</i>	XMM-Newton
Power law	Γ	$1.92^{+0.29}_{-0.36}$	$1.99^{+0.11}_{-0.07}$
	Normalisation ^a	$7.39^{+30.00}_{-4.39}$ ^b	$2.77^{+0.71}_{-0.65}$
Scattered Component	Normalisation ^a	$8.55^{+5.48}_{-4.52} \times 10^{-3}$	$1.62^{+0.29}_{-0.22} \times 10^{-2}$
Absorber	N_H	$2.05^{+4.25}_{-1.38} \times 10^{24} \text{ cm}^{-2}$	$1.0^{+0.1}_{-0.2} \times 10^{23} \text{ cm}^{-2}$
Thermal emission	kT	$0.62^{+0.10}_{-0.17} \text{ keV}$	$0.62^{+0.11}_{-0.11} \text{ keV}$
	Normalisation ^c	$6.94^{+2.40}_{-2.22} \times 10^{-6}$	$3.49^{+1.52}_{-1.50} \times 10^{-6}$
Neutral reflection	Normalisation ^a	$3.46^{+2.14}_{-1.61}$	$3.55^{+1.52}_{-1.81}$
Fe $K\alpha$ ^d	Energy	$6.38^{+0.02}_{-0.02} \text{ keV}$	$6.36^{+0.03}_{-0.03} \text{ keV}$
	EW	$340^{+60}_{-80} \text{ eV}$	$120^{+40}_{-40} \text{ eV}$
	Normalisation ^e	$3.62^{+0.79}_{-0.78} \times 10^{-3}$	$4.75^{+1.35}_{-1.40} \times 10^{-3}$
Ionised Absorber	N_H	..	$6.05^{+8.95}_{-4.10} \times 10^{23} \text{ cm}^{-2}$
	$\log \xi$..	$3.55^{+0.49}_{-0.25} \text{ erg cm s}^{-1}$
	v_{turb}	..	300 km s^{-1}
	χ^2/dof	104.5/103	190.7/197
	F (0.5–2) keV	$\sim 4.9 \times 10^{-14} \text{ erg cm}^{-2} \text{ s}^{-1}$	$\sim 5.8 \times 10^{-14} \text{ erg cm}^{-2} \text{ s}^{-1}$
	F (2–10) keV	$\sim 6.3 \times 10^{-13} \text{ erg cm}^{-2} \text{ s}^{-1}$	$\sim 1.9 \times 10^{-12} \text{ erg cm}^{-2} \text{ s}^{-1}$
	F (14–150) keV	$\sim 1.4 \times 10^{-11} \text{ erg cm}^{-2} \text{ s}^{-1}$	$\sim 1.3 \times 10^{-11} \text{ erg cm}^{-2} \text{ s}^{-1}$
	L (0.5–2) keV	$\sim 4.7 \times 10^{42} \text{ erg s}^{-1}$	$\sim 2 \times 10^{42} \text{ erg s}^{-1}$
	L (2–10) keV	$\sim 7.2 \times 10^{42} \text{ erg s}^{-1}$	$\sim 2.5 \times 10^{42} \text{ erg s}^{-1}$
	L (14–150) keV	$\sim 1.4 \times 10^{42} \text{ erg s}^{-1}$	$\sim 4.8 \times 10^{42} \text{ erg s}^{-1}$

^a units of $10^{-3} \text{ photons keV}^{-1} \text{ cm}^{-2} \text{ s}^{-1}$.^b Due to a degeneracy between the normalisations of the primary power law and PEXRAV, the errors were computed fixing the reflection normalisation to its best-fit value.^c The normalisation of the thermal component is defined as $K = \frac{10^{14}}{4\pi(D_A(1+z))^2} \int n_e n_H dV$ where D_A is the angular diameter distance, z is the redshift, n_e and n_H are the electron and hydrogen density (cm^{-3}) respectively, and dV is the volume from which the deprojected emission originates.^d The line is unresolved; the intrinsic width has been fixed to be $\simeq 10 \text{ eV}$.^e units of $10^{-3} \text{ photons cm}^{-2} \text{ s}^{-1}$.**Figure 4.** Comparison between the *Suzaku* XIS (black, lower spectrum), HXD (black), *Swift*-BAT (green, colors in the electronic version only) and the XMM-Newton (red, upper spectrum) data showing the dramatic change in the curvature in the 3–6 keV energy range. The underlying model (black and green line) is the one obtained fitting only the *Suzaku* XIS (black) and *Swift*-BAT data (green).

Newton spectra, leaving only the absorbing column density (N_H) free to vary. We also left both the cross-normalisation factors between the pn and the MOS spectra and between *Swift*-BAT and pn data free to vary; they were found to be 1.02 ± 0.04 and $1.06^{+0.14}_{-0.16}$ respectively. During the XMM-Newton observation the N_H decreased by about one order of magnitude (from $\sim 2.1 \times 10^{24} \text{ cm}^{-2}$

to $\sim 2.6 \times 10^{23} \text{ cm}^{-2}$); this change in the amount of absorption is sufficient to explain the bulk of the differences between the observed XMM-Newton and *Suzaku* spectra.

For completeness, we also allowed to vary the photon index (Γ), the normalisation of both the power law components, the thermal component and the $K\alpha$ energy and normalisation. The fit yielded $\chi^2/\text{dof}=213.9/199$ and the only parameter changing well beyond the *Suzaku* errors is, as expected, the N_H , decreasing to $2.78^{+0.16}_{-0.17} \times 10^{23} \text{ cm}^{-2}$. This confirms that the strong variation between XMM-Newton and *Suzaku* is due to a change in column density of $\Delta N_H \sim 1.8 \times 10^{24} \text{ cm}^{-2}$.

Prompted from this result we also inspected the 3 *Swift*-X-ray Telescope (XRT) observations taken in 2006 with a time lag of the order of 1–2 days from each other, and we found that the source was in a state similar to that observed by XMM-Newton. The exposure time of each of the observations is less than 10 ksec (8713, 8661 and 3667 sec respectively), thus the relatively low statistics does not allow us to establish if there is a variability between the single observations.

A closer inspection of the residuals in the 5–8 keV energy range to this best-fit model showed some residual curvature between 5 and 6 keV, together with a possible absorption feature centered at $\sim 6.7 \text{ keV}$ (see Figure 5), which is present in both the pn and MOS spectra and is suggestive of a more complex and likely ionized absorber. After checking the significance of this absorption line, we included in the model an additional ionized absorber (see §4.2.1). We note that, after accounting for the absorption feature at $\sim 6.7 \text{ keV}$, the excess of curvature in the range 5–6 keV is not present anymore.

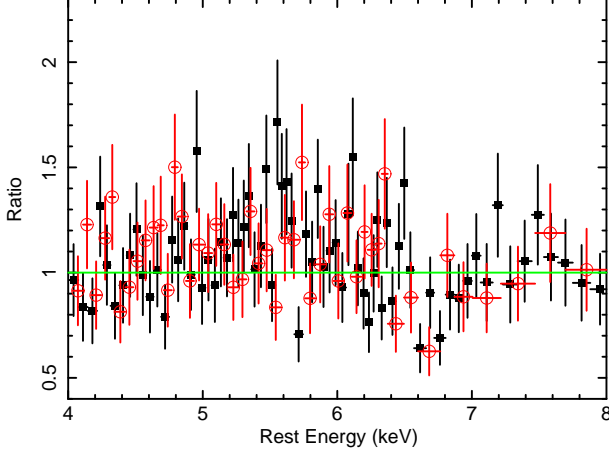


Figure 5. Residuals of the XMM-Newton data (pn data are the black filled squares and MOS data are the red open circles) in the range 4–8 keV with respect to the spectral model discussed in section 4.2. An absorption feature at about 6.7 keV and a spectral curvature in the 5–6 keV range are clearly present.

The parameters of the XMM-Newton best-fit model are reported in table 1 and the final model setup is described in section 4.2.1. We note that the difference in the best-fit normalisations of the thermal and scattering component between *Suzaku* and XMM-Newton are likely due to a degeneracy between these two parameters. Indeed the 0.5–2 keV flux did not strongly vary between the two observations.

The fraction of scattered radiation is $\sim 5\%$. The 2–10 keV flux is $\sim 1.9 \times 10^{-12} \text{ erg cm}^{-2} \text{ s}^{-1}$, while the 2–10 keV luminosity, $L_{(2-10)\text{keV}}$, is $\sim 2.5 \times 10^{42} \text{ erg s}^{-1}$, about a factor 2.8 below the luminosity computed using only the *Suzaku* data. Although such a variation of the intrinsic luminosity is not unusual in AGN, part of this difference could be due to the geometry assumed by the models adopted for the high column density absorber. Indeed we will show in section 4.3 that this difference is smaller (a factor 1.7) when we adopt the *Mytorus* code for the absorber.

4.2.1 The $\sim 6.7\text{keV}$ absorption feature in the XMM-Newton observation

As a first step to model the absorption feature in the 6–7 keV band we added a Gaussian absorbing component; setting $\sigma = 0.05$ keV we found that the centroid of the line is at $E = 6.75^{+0.06}_{-0.04}$ keV, the normalisation is $-3.75^{+1.12}_{-1.13} \times 10^{-6}$ and $\Delta\chi^2 = 24$ for 2 dof. The absorption lines appears to be marginally resolved; however leaving its width free to vary we can set only an upper limit $\sigma < 0.3$ keV, while the energy centroid is found to be consistent within the errors $E = 6.77^{+0.08}_{-0.06}$ keV. The energy of this absorption line suggests an association with absorption from highly ionized Fe (i.e. Fe XXV at $E \sim 6.7$ keV) and thus a clear signature of the presence of an ionized absorber. The presence of an ionized absorber is not exceptional since recent sensitive observations with *Chandra*, XMM-Newton, and *Suzaku* unveiled the presence of red- and blue-shifted photoionized absorption lines both in type 1 and type 2 AGN as well as in Radio Quiet and Radio Loud AGN (Tombesi et al. 2010b, 2011). Thus, it appears that there is a substantial amount of ionized gas in the nuclei of AGNs, which may be linked to gas outflowing on parsec scales with velocities from hundreds of km/s up to $v_{\text{out}} \sim 0.04 - 0.15c$

(Tombesi et al. 2010b). We note that red- and blue-shifted absorption lines are predicted in several theoretical models of failed disk winds (Proga & Kallman 2004; Sim et al. 2010) or of aborted jet (Ghisellini et al. 2004). However, before proceeding with any further modeling of the absorption feature we checked its significance.

To assess the significance of the absorption feature we performed extensive Montecarlo simulations as detailed below. We assumed as our null hypothesis model the best-fit model discussed at the end of section 4.2, and we simulated $S=3000$ spectra (with the *fakeit* command in XSPEC), with the same exposure time as the real data. Each one of these simulated spectra was then fitted with the null hypothesis model to obtain a χ^2 value, and we systematically searched for an absorption line in the 2–10 keV energy range, stepping the energy centroid of the Gaussian in increments of 0.1 keV and refitting at each step. We then obtained for each simulated spectrum a minimum χ^2 and created a distribution 3000 simulated values of the $\Delta\chi^2$ (compared to the null hypothesis model). This indicates the fraction of random generated absorption features in the 2–10 keV band that are expected to have a $\Delta\chi^2$ greater than a threshold value. If N of these simulated values are greater than the real value, then the estimated detection confidence level is $1-N/S$. Using this analysis we can then conclude that the line detection is significant at $>99.97\%$ level.

In order to obtain a physical description of the absorber we replaced the Gaussian absorption line with a model representing a photoionized absorber, which has been produced using a multiplicative grid of absorption model generated with the XSTAR v.2.1 code (Kallman & Bautista 2004). This grid describes an ionized absorber parametrised by its column density (N_{H}), and its ionisation parameter, defined as:

$$\xi = \frac{L_{\text{ion}}}{nR^2} \quad (1)$$

where L_{ion} is the ionising luminosity between 1–1000 Rydbergs (13.6 eV to 13.6 keV), n is the hydrogen gas density in cm^{-3} and R is the radial distance of the absorber from the ionising source. Since there is no apparent broadening of the absorption line we assumed a turbulence velocity of $v_{\text{turb}} = 300 \text{ km s}^{-1}$.

The inclusion of this ionized absorber significantly improved the fit ($\chi^2/\text{dof} = 190.7/197$, $\Delta\chi^2 = 25$ for 2 dof), with a column density of $N_{\text{H}} = 6.05^{+8.95}_{-4.10} \times 10^{23} \text{ cm}^{-2}$ and an ionisation of $\log(\xi/\text{erg cm s}^{-1}) = 3.55^{+0.49}_{-0.25}$. The improvement in the χ^2 is determined solely by fitting the absorption feature in the 6–7 keV band, since an ionised absorber with such a high level of ionization does not produce any feature in the soft band of the continuum.

The parameters of the XMM-Newton best-fit model are reported in table 1 and the setup is the following:

$$\text{WABS} \times [\text{MEKAL} + \text{ZPOWERLW} + \text{ZGAUSS} + \text{ZGAUSS} + \text{PEXRAV} + \text{XSTAR} * \text{CABS} * \text{ZPHABS} \times (\text{ZPOWERLW})]$$

We can now estimate what is the maximum distance of this ionised absorber from the central black hole, using equation 1, relating the ionisation parameter, the density of the absorber and the continuum luminosity L_{ion} . In this case L_{ion} (in the energy range between 13.6 eV and 13.6 keV) is $7.3 \times 10^{42} \text{ erg s}^{-1}$. Assuming that the thickness of the absorber $\Delta R = N_{\text{H}}/n$ is smaller than the distance R_{ion} ($\Delta R/R_{\text{ion}} < 1$), we can set an upper limit to the distance:

$$R_{\text{ion}} = \frac{L_{\text{ion}} \Delta R}{N_{\text{H}} \xi R} < \frac{L_{\text{ion}}}{N_{\text{H}} \xi} = 2.3 \times 10^{15} \text{ cm} \quad (2)$$

This maximum distance of $\sim 10^{-3}$ pc is consistent with a location of the ionised absorber within the Broad Line Region of the AGN. Indeed an estimate of the BLR size R_{BLR} for NGC454E can be inferred by using the relation between R_{BLR} and the monochromatic luminosity at 5100 Å, $L_{5100\text{Å}}$ (Kaspi et al. 2005, $\frac{R_{BLR}}{10 \text{ lt-days}} = 2.45 \times (\lambda L_{\lambda}(5100\text{Å}))^{0.608}$). Since the luminosity of the optical continuum cannot be measured directly from the spectrum, because of the strong absorption, we estimate $L_{5100\text{Å}}$ from the intensity of the [OIII]5007Å line flux, assuming a mean F[OIII]5007Å/F(5100Å) ratio. This ratio has been inferred from the AGN template presented in Francis et al. (1991) ($F(5100\text{Å}) = 0.059F([OIII])$). Using the [OIII]5007Å flux published in Johansson (1988) we obtain $L_{5100\text{Å}} \sim 1 \times 10^{41} \text{ erg s}^{-1} \text{ Å}^{-1}$ and, thus, an approximate size of the BLR of 0.05 pc, i.e. about 50 times R_{ion} .

Since we do not observe this absorption feature in the *Suzaku* spectrum we added to the *Suzaku* best-fit model a gaussian absorption line with the same parameters obtained with the XMM-Newton data. The lower limit for the detection of an absorption line with central energy of 6.75 keV and width of 0.05 keV, is -1.18×10^{-6} for *Suzaku* data. Thus, being the normalisation of this line -3.75×10^{-6} in the XMM-Newton spectrum, we can infer that the ionised absorber should be detectable by *Suzaku*. The simplest interpretation is that also the ionized absorber is variable; which is not surprising since there are several reported cases of variable absorption features (Tombesi et al. 2010b, 2011) (Braitto et al. 2007; Cappi et al. 2009; Dadina et al. 2005; Risaliti et al. 2005). Moreover instability of the outflowing ionized absorbers is predicted both in disk winds models (Proga & Kallman 2004; Sim et al. 2010) or of aborted jet (Ghisellini et al. 2004). This will cause the presence of transient absorption features and variability of the derived outflowing velocities and their EW as observed in several sources (see e.g. Tombesi et al. 2010b).

4.3 A physical interpretation with Mytorus model

The models discussed so far, which are based on spectral components largely used from the astronomical community, do not treat both fluorescent lines and continuum components self-consistently. Furthermore all these spectral components may be deficient in one or more aspect of modelling the complex transmission and reflected spectrum of AGN over a broad energy range and for a large range of absorbing column densities (see section 2 of Murphy and Yaqoob, 2009 for a critical discussion of these points).

In order to alleviate these problems and, thus, to further assess the possible geometry and/or nature of the variable absorber, we tested the most recent model for the toroidal reprocessor⁸ (Murphy & Yaqoob 2009). This model, recently included in the XSPEC software package, is valid for column densities in the range 10^{22} to 10^{25} cm^{-2} and for energies up to 500 keV (the relativistic effects being taken into account); more importantly the reprocessed continuum and fluorescent line emission are treated self-consistently for the first time. This model assumes that the absorber geometry is toroidal with an opening angle of 60° . Since we are clearly seeing a variation of the absorbing column density along the line of sight we have used a spectral configuration of *MyTorus* that can *mimic* a clumpy absorber and which also takes

into account the fact that the Fe K α is rather constant (see table 1).

We have done this by decoupling the line-of-sight continuum passing through the reprocessor (or zeroth order continuum, see <http://www.mytorus.com/manual/index.html>) and the reflected (or scattered continuum, see mytorus model) continuum from reprocessor. In practice we allowed the column densities of the line-of-sight continuum and scattered-reflected continua to be independent of each other. The reflected continuum, and the fluorescent line emission which is consistently produced in the same location, is not extinguished by another column of intervening matter. Since the XMM-Newton spectrum unveiled the presence of an additional ionized absorber, which affects the line-of-sight continuum we also included an ionized absorber, which is modelled adopting the same XSTAR grid as described in section 4.2.1. In order to do that, we disentangled the absorbing column density of the line-of-sight (los) component from that for the scattered continuum plus fluorescent emission lines. The inclination angle of the los component has been fixed at 90 degrees; the inclination angle for the reflected/ scattered continuum plus line component component was, for simplicity, fixed at 0 degrees since the effect of the inclination angle on the shape of the scattered continuum is not sufficiently large when the scattered continuum is observed in reflection only. Physically, the situation we are modelling by means of this decoupling could correspond to a patchy reprocessor in which the scattered continuum is observed from reflection in matter on the far-side of the X-ray source, without intercepting any other “clouds,” while the intrinsic continuum is filtered by clouds “passing” through our line-of-sight to the central engine.

We applied this model to the the XMM-EPIC and *Swift*-BAT spectra and we found a good fit with the same absorbing column density ($N_H = 2.75^{+0.05}_{-0.04} \times 10^{23} \text{ cm}^{-2}$; $\chi^2/\text{dof}=201/192$) filtering the line-of-sight intrinsic continuum and producing the scattered component (including the production of the fluorescent emission lines). The parameters of the ionized absorber are: $N_H = 6.46^{+5.04}_{-1.96} \times 10^{23} \text{ cm}^{-2}$ and $\log \xi = 3.26^{+0.20}_{-0.21} \text{ erg cm s}^{-1}$; these values are in good agreement with those found with the best-fit model described in table 1. The photon index of the primary power-law component is now $\Gamma = 1.86^{+0.11}_{-0.17}$ and the intrinsic emitted luminosity is $L_{[2-10]\text{keV}} \sim 1.4 \times 10^{42} \text{ erg s}^{-1}$. Using the *Suzaku* and *Swift* data, we found that a good fit can be obtained with an absorber producing the reflected components having an N_H statistically consistent with that obtained using the XMM-Newton data (thus suggesting that this component is likely associated with the distant reflector or torus), while our line of sight to the central engine intercepts a column density $N_H = (0.88 \pm 0.09) \times 10^{24} \text{ cm}^{-2}$.

In summary this analysis, which is based on a model which takes into account consistently the physical process in place within the X-ray absorber, shows that the change of state of NGC454E can be understood simply by a chance change in the line-of-sight obscuration ($\Delta N_H \sim 6 \times 10^{23} \text{ cm}^{-2}$) while the global obscurer remains unchanged. The intrinsic luminosity derived from the *Suzaku* data is $L_{[2-10]\text{keV}} \sim 2.4 \times 10^{42} \text{ erg s}^{-1}$. We note that using *MyTorus* the derived change of the intrinsic luminosity between the two data sets are in better agreement (a factor 1.7) with respect to those found in section 4.2. However, with the present statistic and the complexity of the observed spectra, we cannot rule out or confirm a possible variation in luminosity of about a factor 2, frequently observed in AGN; indeed by comparing the 54-months and 9-months BAT high energy (14–195 keV) spectra of this source, we found that the intensity is higher in the 9-months spectrum. However, fitting the spectra with a single absorbed power-law component, we

⁸ <http://www.mytorus.com/>

found that a constant flux is also well within the errors on the best-fit normalizations of this primary power-law.

5 SUMMARY AND CONCLUSION

We have presented the results of *Suzaku*, *XMM-Newton* and *Swift* observations of the interacting system NGC454 ($z=0.0122$). The bulk of the measured 2–10 keV emission comes from the active galaxy NGC454E ($L_{[2-10]\text{keV}} \sim 2 \times 10^{42} \text{erg s}^{-1}$); no emission from the center of the companion galaxy (NGC454W) in the interacting system is detected. The nuclear X-ray emission of NGC454E is filtered by an absorbing column density typical of a Seyfert 2 galaxy, in agreement with the optical classification.

A comparison between *Suzaku* and *XMM-Newton* observations (taken 6 months later) revealed a significant change in the spectra of NGC454E in the energy range between 3 and 6 keV. This variation can be well explained by a variability of about an order of magnitude in the absorbing column density along the line of sight: from $\sim 1 \times 10^{24} \text{cm}^{-2}$ (*Suzaku*) to $\sim 1 \times 10^{23} \text{cm}^{-2}$ (*XMM-Newton*). This study also adopted the most recent model for the toroidal reprocessor (Murphy & Yaqoob 2009), which takes into account consistently the physical processes in place within the X-ray absorber. Furthermore, regarding the *XMM-Newton* spectrum, we detected a statistically significant absorption feature at ~ 6.7 keV, a clear signature of the presence of a ionised absorber, with ionisation parameter $\log(\xi/\text{erg cm s}^{-1}) = 3.55$ and column density $N_{\text{H}} = 6.05 \times 10^{23} \text{cm}^{-2}$. The absence of this feature in the *Suzaku* spectrum, despite its detectability, implies that it has varied between the two observations. Absorption lines associated with ionized iron have been now observed in several sources and there is also a clear evidence that these lines are variable as in the case of NGC454. Furthermore, in some cases the measured blue-shifts of the energy centroids imply a large velocity of these absorbers and a likely association with powerful disk winds (King & Pound 2003), while in other cases there is no measurable motion as in our case.

In summary, with respect to the absorbing column density variability, NGC454E is a new member of the class of “changing look” AGN, i.e. AGN that have been observed in both Compton-thin ($N_{\text{H}}=10^{23} \text{cm}^{-2}$) and reflection dominated states ($N_{\text{H}} > 10^{24} \text{cm}^{-2}$). A possible scenario is that a stable and likely distant absorber responsible for the iron emission line is present. However, there is also a clear variation of the N_{H} of the line of sight absorber, probably indicative of the clumpy nature of the rather neutral absorber itself. Unfortunately the comparison between different observations, typically performed at intervals of months to years (as those discussed here), provides only upper limits to the intrinsic time scales of N_{H} variations and thus on the possible location of the thicker obscuring material (obscuring “torus” vs. Broad Line Region clouds). The low exposure of the *Swift* XRT 2006 observations, when the source was in a state similar to the *XMM-Newton* one, did not allow us to establish the N_{H} variability on smaller time scales (i.e. intra-day) of the single observations. An improvement of the estimates of velocity, distance and size from the central X-ray source of the obscuring material could be obtained only through monitoring observational campaigns within a few days or weeks and/or through the search for N_{H} variations within single long observation. For what concerns the ionised absorber, as derived from our first order estimate

of its distance from the central black hole (i.e. within 10^{-3} pc), the most likely location for this absorber is much closer in than the stable and rather neutral one.

ACKNOWLEDGEMENTS

We warmly thank T. Yaqoob for the useful discussion and for helping us while fitting the *Mytorus* model to mimic the variable absorber. We thank the anonymous referee for many useful suggestions and comments that significantly improved the paper. This research has made use of data obtained from the *Suzaku* satellite and data obtained from the High Energy Astrophysics Science Archive Research Center (HEASARC), provided by NASA’s Goddard Space Flight Center. The authors acknowledge financial support from ASI (grant n. I/088/06/0, COFIS contract and grant n. I/009/10/0). VB acknowledges support from the UK STFC research council.

REFERENCES

- Antonucci, R. 1993, ARA&A, 31, 473
- Arp, H. C., & Madore, B. F. 1987, A Catalogue of Southern Peculiar Galaxies and Associations (Cambridge: Cambridge Univ. Press)
- Baumgartner et al, 2011 ApJS, submitted
- Bianchi, S., Guainazzi, M., Matt, G., et al. 2005, A&A, 442, 185
- Bianchi, S., Piconcelli, E., Chiaberge, M., Bailòn, E. J., Matt, G., & Fiore, F. 2009, ApJ, 695, 781
- Boldt, E. 1987, Phys. Rep., 146, 215
- Braito, V., Reeves, J. N., Dewangan, G. C., George, I., Griffiths, R. E., Markowitz, A., Nandra, K., Porquet, D., Ptak, A., Turner, T. J., Yaqoob, T., & Weaver, K., 2007, ApJ, 670, 978
- Cappi, M., Tombesi, F., Bianchi, S., et al. 2009, A&A, 504, 401
- Cusumano G., La Parola V., Segreto A., Ferrigno C., Maselli N., Sbarufatti B., Romano P., Chincarini G., Giommi P., Masetti N., Moretti A., Parisi P., Tagliaferri G., 2010, A&A, 524, A64
- Dadina, M., Cappi, M., Malaguti, G., Ponti, G., & de Rosa, A. 2005, A&A, 442, 461
- Dadina, M. 2008, A&A, 485, 417
- Della Ceca, R., Ballo, L., Tavecchio, F., et al. 2002, ApJ, 581, L9
- den Herder, J. W., et al. 2001, A&A, 365, L7
- Dickey, J. M., & Lockman, F. J. 1990, ARA&A, 28, 215
- Done C., 2010, arXiv, arXiv:1008.2287
- Ehle, M., et al. 2001, XMM-Newton Users Handbook
- Elvis, M., Risaliti, G., Nicastro, F., Miller, J. M., Fiore, F., & Puccetti, S. 2004, ApJ, 615, L25
- Fabian, A. C. 2010, IAU
- Francis P. J., Hewett P. C., Foltz C. B., Chaffee F. H., Weymann R. J., Morris S. L., 1991, ApJ, 373, 465 Symposium, 267, 341
- Gruber, D. E., Matteson, J. L., Peterson, L. E., & Jung, G. V. 1999, ApJ, 520, 124
- Gehrels, N., Chincarini, G., Giommi, P., et al. 2004, ApJ, 611, 1005
- Ghisellini, G., Haardt, F., & Matt, G. 2004, A&A, 413, 535
- Jansen, F., et al. 2001, A&A, 365, L1
- Johansson, L. 1988, A&A, 191, 29
- Kaastra, J. S. & Mewe, R. 1993, A&AS, 97, 443
- Kallman, T. R., Palmeri, P., Bautista, M. A., Mendoza, C., & Krolik, J. H. 2004, ApJS, 155, 675

- Kaspi, S., Maoz, D., Netzer, H., et al. 2005, *ApJ*, 629, 61
- King, A. R., & Pounds, K. A. 2003, *MNRAS*, 345, 657
- Kokubun, M., et al. 2007, *PASJ*, 59, 53
- Koyama, K., Tsunemi, H., Dotani, T., et al. 2007, *PASJ*, 59, 23
- Lobban, A. P., Reeves, J. N., Miller, L., et al. 2011, *MNRAS*, 414, 1965
- Magdziarz, P., & Zdziarski, A. A. 1995, *MNRAS*, 273, 837
- Mateos S. et al., 2008, *A&A*, 492, 51
- Mewe, R., Gronenschild, E.H.B.M., and van den Oord, G.H.J. 1985, *A&AS*, 62, 197
- Murphy, K. D., Yaqoob, T., & Terashima, Y. 2007, *ApJ*, 666, 96
- Murphy, K. D., & Yaqoob, T. 2009, *MNRAS*, 397, 1549
- Mitsuda, K., et al. 2007, *PASJ*, 59, 1
- Pounds, K. A., Reeves, J. N., Page, K. L., & O'Brien, P. T. 2004, *ApJ*, 616, 696
- Proga, D., & Kallman, T. R. 2004, *ApJ*, 616, 688
- Puccetti, S., Fiore, F., Risaliti, G., Capalbi, M., Elvis, M., & Nicastro, F. 2007, *MNRAS*, 377, 607
- Ross & Fabian (2005), *MNRAS*, 358, 211
- Risaliti, G., Elvis, M., & Nicastro, F. 2002, *ApJ*, 571, 234
- Risaliti, G., Elvis, M., Fabbiano, G., Baldi, A., & Zezas, A. 2005, *ApJ*, 623, L93
- Risaliti, G., Elvis, M., Fabbiano, G., Baldi, A., Zezas, A., & Salvati, M. 2007, *ApJ*, 659, L111
- Risaliti, G., et al. 2009, *ApJ*, 696, 160
- Risaliti, G. 2010, in American Institute of Physics Conference Series, Vol. 1248, American Institute of Physics Conference Series, ed. A. Comastri, L. Angelini, & M. Cappi, 351354
- Risaliti G., Elvis M., Bianchi S., Matt G., 2010, *MNRAS*, 406, L20
- Shu, X. W., Yaqoob, T., Murphy, K. D., et al. 2010, *ApJ*, 713, 1256
- Sim, S. A., Proga, D., Miller, L., Long, K. S., & Turner, T. J. 2010, *MNRAS*, 408, 1396
- Spergel, D. N., et al. 2003, *ApJS*, 148, 175
- Stiavelli, M., Panagia, N., Carollo, M.C., Romaniello, M., Heyer, I., Gonzaga, S. 1998, *ApJ* 492, L135
- Strüder, L., et al. 2001, *A&A*, 365, L5
- Takahashi, T., et al. 2007, *PASJ*, 59, 35
- Tombesi F., Cappi M., Reeves J. N., Palumbo G. G. C., Yaqoob T., Braitto V., Dadina M., 2010, *A&A*, 521, 57
- Turner, T. J., Miller, L., Kraemer, S. B., Reeves, J. N., & Pounds, K. A. 2009, *ApJ*, 698, 99
- Tombesi F., Cappi M., Reeves J. N., Palumbo G. G. C., Braitto V., Dadina M., 2011, *ApJ* accepted
- Turner, M., et al. 2001, *A&A*, 365, L27
- Turner T.J., Miller L., 2009, *A&ARv*, 17, 47
- Uttley, P., Taylor, R. D., McHardy, I. M., et al. 2004, *MNRAS*, 347, 1345
- Weaver, K. A., Nousek, J., Yaqoob, T., et al. 1996, *ApJ*, 458, 160
- Wilms, J., Allen, A., & McCray, R. 2000, *ApJ*, 542, 914
- Yaqoob, T. 1997, *ApJ*, 479, 184